DE GRUYTER

Methods in Microscopy 2025; aop

Research Article

Murilo I. Santos, Juliana M. de Souza e Silva, Daina Damberga, Markus Langner, Rafaela Debastiani, Ulrike Hirsch, Andreas Greiner and Ralf B. Wehrspohn*

Visualizing and simulating composite filtration mats: a study using X-ray microscopy and fluid flow simulations

https://doi.org/10.1515/mim-2025-0005
Received March 12, 2025; accepted August 29, 2025;

Abstract: Our research focuses on verifying the design of efficient composite filtration mats using simulations based on XRM volumetric data. Three filter mats were prepared with different amounts of PET microfibers and electrospun PAN nanofibers, with and without a diblock copolymer. The structure of the PET-PAN mats was characterized by SEM and XRM. Three-dimensional XRM images were used in fluid flow simulations and the filtration properties were evaluated by standard methods. Incorporating 5-μm PET fibers with 1 wt% PAN nanofibers and a diblock copolymer doubled efficiency in single-pass filtration test at a small pressure drop. Raising PAN to 2 wt% increased efficiency to 72 % but also increased the pressure drop. Simulated permeabilities from XRM volumes follow the same order and lie within experimental uncertainties. Streamlines illustrate fluid flow paths within the simulated environment, showing locations where fiber bundles create straight-through pores. XRM simulations showed flow paths, confirmed permeability trends, and can guide the optimization of fiber dispersion. Discrepancies between XRM volumes and bulk tests show that microscale heterogeneity dominates resistance. Larger volumes are needed for accurate prediction. Streamline-guided rules can shorten development cycles by indicating where to adjust fiber orientation, nanofiber amounts and copolymer amounts.

Keywords: X-ray microscopy; XRM; fluid flow simulations; electrospinning; filtration

1 Introduction

The development of alternative filtration materials is essential to meet the growing demand for efficient air and water purification systems in the residential, healthcare, and industrial sectors [1], [2]. As energy consumption concerns continue to rise, novel filtration materials must balance high particle capture efficiency with minimal pressure drop to reduce operating costs while maintaining performance [3]. Achieving this balance requires careful selection of materials, optimization of pore structures, and refinement of manufacturing techniques [4], as well as a thorough understanding of the relationship between their microstructure and filtration properties.

Microstructural information can be obtained with traditional two-dimensional (2D) imaging techniques, such as scanning electron microscopy (SEM) and optical microscopy. They provide detailed information about the surface morphology of the filtration materials [5], [6], relevant to particle capture efficiency and pressure drop. However, these 2D imaging techniques have limitations in providing a comprehensive understanding of the microstructure of filtration materials, particularly in terms of their three-dimensional (3D) pore structure and connectivity, leading to difficulties in predicting their filtration performance and optimizing their design [7]. Advanced three-dimensional (3D) imaging techniques, such as X-ray microscopy (XRM) and focused ion beam-scanning electron microscopy (FIB-SEM), have emerged as essential

---

***Corresponding author: Ralf B. Wehrspohn**, Institut für Physik - Martin-Luther-Universität Halle-Wittenberg, Heinrich-Damerow-Str. 4, 06120 Halle, Germany, E-mail: ralf.wehrspohn@physik.uni-halle.de

Murilo I. Santos and Juliana M. de Souza e Silva, Institute of Physics, Martin Luther University of Halle-Wittenberg, Halle, Germany

Daina Damberga and Andreas Greiner, Macromolecular Chemistry and Bavarian Polymer Institute, University of Bayreuth, Bayreuth, Germany

Markus Langner, BinNova Microfiltration GmbH, Rudolstadt, Germany

Rafaela Debastiani, Institute of Nanotechnology (INT), Karlsruhe Institute of Technology (KIT), Karlsruhe, Germany; and Karlsruhe Nano Micro Facility (KNMFi), Karlsruhe Institute of Technology (KIT), Eggenstein-Leopoldshafen, Germany

Ulrike Hirsch, Fraunhofer Institute for Microstructure of Materials and Systems IMWS, Halle, Germany

tools for characterizing the complex microstructure of filtration media [8], [9]. These techniques enable the visualization of the intricate pore networks, fiber orientations, and surface features of filter media, allowing for a more accurate understanding of their filtration mechanisms and performance characteristics.

FIB-SEM enables high-resolution 3D imaging with isotropic resolution at the nanoscale, but it is limited by slower imaging speeds, small volumes, potential artifacts during reconstruction (e.g., sample drift and shine-through effects), and its destructive nature. In contrast, 3D XRM offers non-destructive imaging with higher throughput and larger field of view, but at lower resolutions compared to FIB-SEM. XRM is particularly advantageous for studying larger volumes or internal structures with features larger than a few hundred nanometers [10], [11] in virtual cross-sections in any direction, which would otherwise require extensive sample preparation and labor-intensive analyses. In particular, phase-contrast XRM enhances the study of materials with inherently low X-ray attenuation, such as polymer fibers, without any complicated preparation protocol [12], [13] and provides highly detailed quantitative data on structural parameters known to influence filtration performance, including porosity, pore size distribution, fiber diameter, and tortuosity [14]. Beyond structural characterization, 3D imaging allows the absolute permeability of filter materials to be evaluated through numerical simulations. This parameter is a measure of how easily a fluid flows through a porous medium under a pressure gradient [15]. Understanding these characteristics is critical to establishing structure-function relationships between a filter material, its permeability to a fluid, and its filtration efficiency [16].

Here we used SEM and phase-contrast XRM to visualize the fiber morphology and distribution of fibers in 2D and 3D, to investigate the structural and filtration properties of three composite fiber filter mats composed of polyethylene terephthalate (PET) microfibers and electrospun polyacrylonitrile (PAN) nanofibers to produce a fine pore structure with high filter efficiency [17]. These mats were produced with varying PAN content, with and without a diblock copolymer added to enhance the dispersion of the PAN nanofibers. Based on the 3D XRM datasets obtained, we aimed to test whether a small XRM volume can be used to predict bulk permeability of the filters. Thus, we performed fluid flow simulations to analyze the internal flow streamlines and examine how variations in fiber arrangement and porosity influence the permeability in the PET-PAN mats. Furthermore, we compared the simulation results with those of laboratory filtration tests to evaluate filtration efficiency and determine the conditions under which 3D XRM data could be used to understand the structure-property relationships and inform the future design of efficient composite mats.

2 Materials and methods

2.1 Materials

Polyethylene terephthalate (PET) fibers of type 309NSD (0.5 dtex, 5 mm) and 271P (2.2 dtex, 6 mm, polyester sheath) were provided by ADVANSA GmbH (Hamm, DE). Polyacrylonitrile (PAN, $M_w = 304{,}000$ g/mol) was purchased from DOLAN GmbH (Kelheim, DE) and BX9 micro-fine glass fibers from Alkegen (USA). Dimethylformamide (DMF) was purchased from Sigma Aldrich (Saint Louis, MO, USA). Ammonia solution (9 vol%) and sulfuric acid were purchased from Carl Roth GmbH + Co. KG (Karlsruhe, DE). A custom-synthesized amphiphilic diblock copolymer, denoted as poly(acrylic acid)-block-(n-butyl acrylate) (poly(AA_{94}-block-nBA_{58})), where the subscript numbers indicate the degree of polymerization for the acrylic acid (94 units) and n-butyl acrylate (58 units) blocks, respectively ($M_n = 14{,}000$ g/mol, abbreviated to DBCP) was kindly provided by Rika Schneider from the University of Bayreuth. The copolymer was prepared via a multi-step synthesis route. First, a poly(tert-butyl acrylate) macroinitiator was synthesized. This was then chain-extended with n-butyl acrylate to form the precursor diblock copolymer, poly(tBA_{94}-b-nBA_{58}). This precursor exhibited a narrow molecular weight distribution with a dispersity (Đ) of 1.13. Finally, a selective acidolysis was performed to convert the tert-butyl groups into carboxylic acid groups, yielding the target amphiphilic DBCP with a final theoretical number-average molecular weight of approximately 1.4×10^4 Da. Full details of the synthesis protocol and comprehensive characterization data are provided in the Supporting Information (Figs. S1–S4).

2.2 Fiber fabrication and filter mat wet-laid fabrication

2.2.1 PAN fiber preparation

PAN non-woven fibers were prepared by electrospinning of a 14 wt% PAN solution in DMF. The electrospun fiber mat was cut into smaller pieces and suspended at a concentration of 3.7 g/L in an isopropanol:water solution (1:1, v/v). The fiber-solvent mixture was then frozen in a slurry state using liquid N_2 (−196 °C) and the short fibers were obtained by blending the mixture using a blender

Table 1: Composition of PET-PAN filters prepared with different fiber and DBCP ratios.

Sample	PET (309NSD) (wt%)	PET (271p) (wt%)	PAN nanofibers (wt%)	DBCP (wt% with respect to fiber)
PET-PAN-A	79	20	1	0
PET-PAN-B	79	20	1	0.1
PET-PAN-C	78	20	2	0.1

(Blixer 6 VV, Robot Coupe, Vincennes – FR, or SB-7020, Steinborg, Nufringen – DE). The resulting short fiber suspension was then used in the following steps.

2.2.2 PET-PAN filter wet-laid fabrication

PET-PAN filter mats were prepared with three different ratios (Table 1). In a typical preparation, the required amount of PET fibers (ca. 78 % 309NSD and 20 % 271P) were dispersed in 2.5 L of a 0.0001 N H_2SO_4 ($pH = 3$) aqueous solution in a dispersion unit operating at 3,000 rpm for 1 min. Stirring was reduced to 1,000 rpm, then PAN nanofibers (ca. 0.1 g – 2 wt% as dispersion) were added. When required, 5 mL of a 1 mg/mL DBCP aqueous solution ($pH = 9$, adjusted with NH_4OH) were added to the mixture. After 5 min, the dispersions were divided into 1 L portions for the wet-laid fabrication. Each portion was mixed with an additional 5 L of water at $pH = 3$ and poured into a column with a 20 cm diameter, 300-mesh stainless steel column sieve placed on the bottom to drain off the water (hand sheet former BB, Estanit GmbH, Mühlheim, DE). The resulting wet sheet was aspirated with a slight vacuum and transferred from the sieve to silicone paper for drying.

2.3 Scanning electron microscopy imaging

The surface morphology of the PET-PAN filters was analyzed using a Quanta 3D FEG scanning electron microscope (Thermo Fisher Scientific/FEI). All samples were mounted on standard SEM holders, and a thin platinum layer was applied to prevent surface charging. Image acquisition was carried out in secondary electron (SE) mode at an accelerating voltage of 5 kV. Pristine PET and PAN fiber diameters were measured using ImageJ [18] and diameter distributions obtained are presented as histograms.

2.4 Three-dimensional X-ray imaging

Each sample was cut into squares of approximately 2 mm × 2 mm using a scalpel. Superglue was applied to one corner and the sample was attached to the tip of a metal pin. Imaging was performed using a Carl Zeiss Xradia 810 Ultra (Pleasanton, CA, USA) X-ray microscope equipped with a rotating chromium anode operating at a fixed photon energy of 5.4 keV. A total of 1,001 projections were collected over a range of 180° (+90° to −90°) with a minimum exposure time of 10 s per projection. Imaging was performed in large field-of-view mode ($64 \times 64\ \mu m^2$) using a Zernike phase ring to acquire phase-contrast images. To increase pixel readout speed, the camera binning was set to 2, resulting in a voxel size of 128 nm in the final images. Projections were reconstructed by filtered back projection using XMReconstructor software (Carl Zeiss). Two datasets were imaged from each sample with a vertical overlapping region of a few microns. Datasets were exported as a stack of 16 bit tiff images for stitching (to a size of ca. 64 μm × 64 μm × 115 μm) and further processing.

2.5 Image processing and quantitative analyses

Stacks of virtual slices were automatically adjusted for brightness and contrast using ImageJ (v1.54f, National Institutes of Health – NIH, USA) [18] and exported as 8 bit images. The resulting corrected datasets were used in the segmentation of PAN nanofibers. In addition, for segmentation of PET fibers, a single-distance phase-retrieval algorithm (Paganin method) [19] was applied on the virtual slices using the ANKAphase plugin [20] for ImageJ to retrieve the information on the interior of the PET fibers and was configured with a Gaussian width of 1 pixel and a stabilizer value of 0.2 for image restoration. The energy was set to 5.4 keV, with a detector distance of 1,000 mm and a pixel size of 1 μm. The δ/β ratio was empirically determined within the range of 0.25–5 (Figure S5). Brightness and contrast of the datasets were then adjusted in the resulting images, which were further processed in Avizo (version 9.7.0, Thermo Fisher Scientific, Germany) for image segmentation. PAN and PET fibers were segmented (respectively from the original datasets, and after Paganin phase retrieval) using an interactive thresholding method based on gray-level intensities or a watershed segmentation. The resulting binarized datasets were further processed to remove small artifacts and to smooth the surfaces of the fibers using a Gaussian filter. PAN and PET thickness distributions were determined after skeletonization using Avizo centerline tree module (optimized with a slope of −2.5 and zeroVal of 20 for PAN and 10 for PET fibers, respectively). Additionally, the volume fraction was obtained from the entire volume and centroid path tortuosity module was used to estimate the tortuosity of the empty path. Here, the tortuosity factor (τ) is defined as the ratio of the effective path length (length of the convoluted pathway) of the pores and the straight-line distance between start and end of path.

2.6 Absolute permeability simulation on PET-PAN mats

The absolute permeability (k) of the filter media to air was simulated using the Absolute Permeability Experiment Simulation module in the Avizo XLabSuite Extension, which uses a finite volume method to solve the Stokes' equation systems [21]. Absolute permeability appears in Darcy's law as a constant coefficient relating fluid, flow and material parameters (Eq. (1)):

$$\frac{Q}{S} = -\frac{k}{\mu}\frac{\Delta p}{L} \tag{1}$$

where Q is the volumetric flow rate through the porous sample, S is the cross section of the sample perpendicular to the flow, k is the absolute permeability of the medium (sample), μ is the dynamic viscosity of the fluid (equal to ρv_D, where ρ is the fluid density and v_D is Darcy velocity), Δp is the pressure drop across the sample, and L is thickness of the sample in the flow direction. $\frac{Q}{S} = \upsilon_D$ is Darcy velocity (superficial or face velocity), which is the mean fluid flow velocity through the porous sample. Simulations were conducted in cuboid-shaped subvolumes (25.5 μm × 38.4 μm × 25.5 μm) with volumetric flow rate (Q) of 3.44×10^7 μm^3/s, corresponding to a v of 5.3 cm/s through an area (S) of approximately 650 μm^2 to find the simulated absolute permeability (k_{sim}) for the samples. In all simulations, the inlet pressure was set to 1.0×10^5 Pa, and the dynamic viscosity (μ) of air at 25 °C was defined as 1.8213×10^{-5} Pa s. In the simulation of an experiment, four faces are hermetically closed while experimental setups are added on two opposite faces to guide the flow along one direction [21]. The flow direction was set orthogonal to the fibers along the y-axis to ensure correlation with the experimental setup. Simulations were performed with $n \geq 3$ subvolumes and the standard deviation is given.

2.7 Filtration tests

The performance of the filter was evaluated using a filter testing station (MFP 2000, Palas GmbH, Karlsruhe, Germany) with bis(2-ethylhexyl) sebacate (DEHS) as the aerosol model. Ultra-fine glass fibers (BX9) were used as a reference, as these fall within the submicron range as do the PAN nanofibers. Testing was conducted over a filtration area (S) of 100 cm^2 with a face velocity of 5.3 cm/s for 180 s, and the aerosol particles used for testing ranged in size from 0.124 to 2.738 μm. To provide statistically relevant results, a total of 32,000 particles were measured per test. Background measurements were performed prior to each test to ensure accuracy, and the pressure drop (Δp) was recorded both at the beginning and end of each measurement for each sample. Measurements were conducted in triplicates to ensure statistical significance.

Filtration efficiency was measured at a particle size of 0.3 μm, which was used as the standard for all measurements, using Eq. (2):

$$\text{Efficiency (\%)} = \left(1 - \frac{C_{\text{down}}}{C_{\text{up}}}\right) \times 100 \tag{2}$$

where C_{up} is the particle concentration upstream of the filter, and C_{down} is the particle concentration downstream.

The permeability constant (k_{exp}) was determined by solving the equation for the discharge coefficient (C_D) for flow through a porous mat [22], which is given in Eq. (3):

$$C_D = \frac{\Delta p}{\rho.\nu \cdot \upsilon_D} = \frac{s}{k_{\text{exp}}}, \tag{3}$$

where Δp is the pressure drop, ρ is the density of the working fluid, ν is the kinematic viscosity of the fluid ($\nu = \frac{\mu}{\rho}$), v_D is the Darcy velocity (superficial or face velocity), s is the specific surface area of the fiber network, k_{exp} is the experimental permeability constant obtained from Darcy's law ($k_{\text{exp}} = \frac{\mu \upsilon_D L}{\Delta p} = \frac{\rho.\nu\left(\frac{Q}{S}\right)L}{\Delta p}$) using the following constants for air at 25 °C: working fluid (air) density (ρ) = 1.169 kg/m^3, and kinematic viscosity (ν) = 15.58 mm^2/s and volume flow of 31.8 L/min. Volumetric flow rate (Q) was set at 0.0533 m/s for a filter cross-sectional area (S) of 100 cm^2 and thickness (L) of 0.038 mm.

3 Results

To prepare the three different PET-PAN mats studied in this work, we first produced the PAN nanofiber suspension. For that, PAN non-woven nanofibers were prepared by electrospinning, resulting in a mat that was then cut

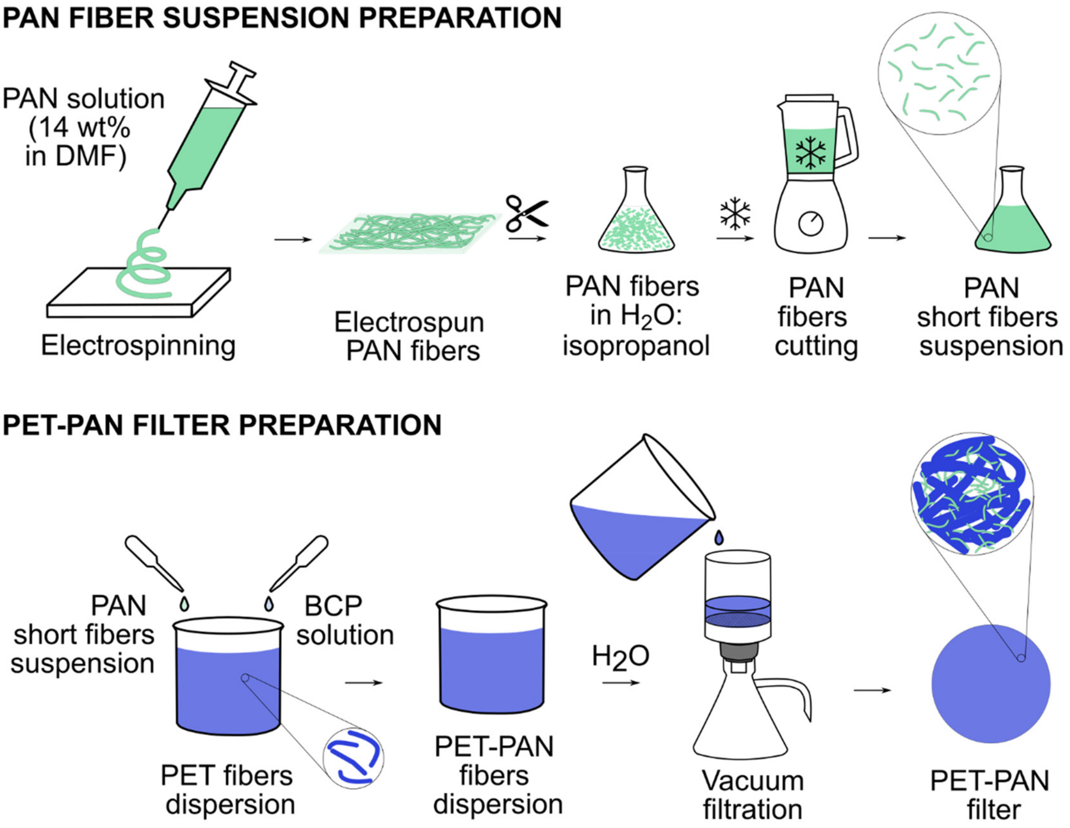

Figure 1: Sketch showing the steps for preparation of the wet-laid filters used in this study.

into smaller pieces (Figure 1). The resulting suspension of short PAN nanofibers was mixed with dispersed PET fibers and diblock copolymer, if required, and then wet-laid to prepare the filter mats. The three PET-PAN composite mats fabricated contained either 1 wt% of PAN (PET-PAN-A, and PET-PAN-B) or 2 wt% (PET-PAN-C). Depending on the formulation, they contained a diblock copolymer (DBCP) made of acrylic acid and n-butyl acrylate (PET-PAN-B and PET-PAN-C). The DBCP used in this study, poly(acrylic acid)-block-(n-butyl acrylate), was chosen for its amphiphilic character [23] (Table 1) and its ability to adjust the surface charge and surface energy of the hydrophobic electrospun nanofibers, stabilizing PAN nanofibers dispersed in water prior to the wet-laying process.

The PET has straight, coarse fibers (Figure 2A), and the electrospun PAN forms a dense web of randomly oriented thin nanofibers (Figure 2B). The fiber thickness distribution obtained from the SEM images shows that the thickness of the PET fibers is centered at 5.37 ± 0.08 μm and that of PAN at 0.26 ± 0.08 μm. SEM images of the PET-PAN composites (Figure 3A–C) reveal a thick PET fiber structure forming a closed mesh, which is overlaid with PAN nanofibers filling selected regions. The difference in the amount of PAN among the samples is not evident from the images.

This heterogeneity of PAN nanofibers distribution is also observed in the XRM images (Figure 3D–I), which reveal complex networks of PAN nanofibers surrounding the thicker PET fibers throughout the mats' volume. The distribution of PAN nanofibers revealed large gaps between the PET fibers, indicating incomplete PAN coverage. This is evident even at the highest 2 % PAN concentration, where some areas were completely covered by PAN nanofibers, while others remain uncovered and featured large pores without PAN. Further analysis of the images revealed differences in the PAN fiber agglomeration across the samples. In PET-PAN-A, PAN fibers predominantly adhere to the PET fiber surface (Figure 3D and G), while in PET-PAN-C (Figure 3F and I), a more extensive coverage of PET fibers by PAN nanofibers is observed. This observation is consistent with the increasing PAN content in the filter mats. These findings are summarized in the Table 2, which provides a comprehensive comparison of the morphological characteristics as observed by SEM and XRM for each filter composition.

We used the volumetric XRM datasets to perform a quantitative analysis of the PET-PAN mats (Figure 4, Table 3). The thicknesses of PET and of PAN are consistent across all samples at 5–6 μm and 0.33–0.36 μm, respectively

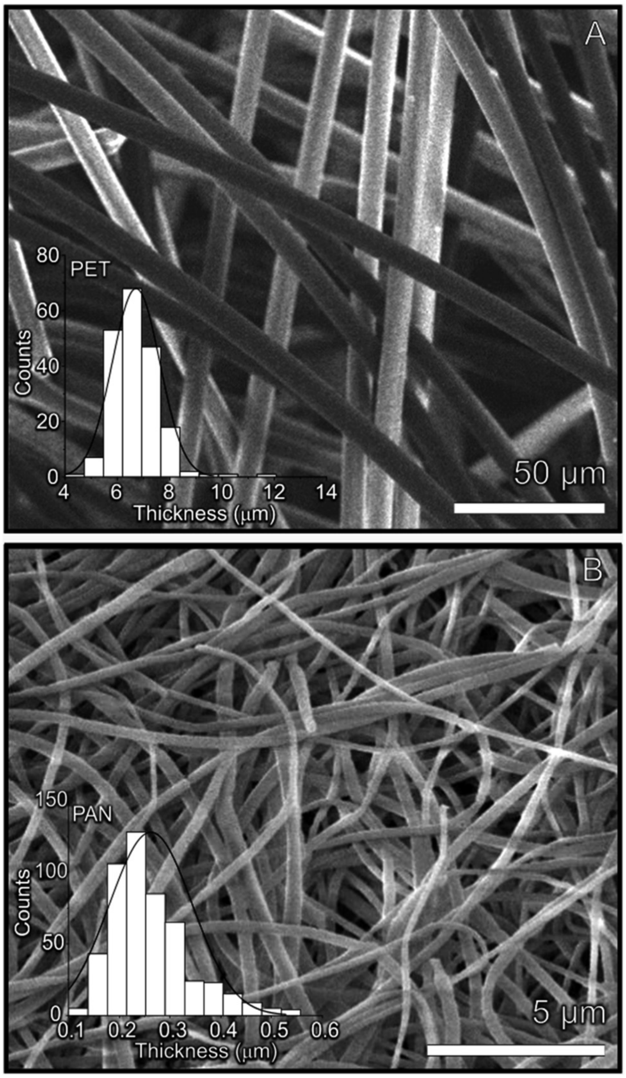

Figure 2: SEM images of pristine materials used for the preparation of the PET-PAN composite filter mats: (a) PET fibers and (b) electrospun mat of PAN nanofibers.

(Figure S6). The PET fiber count for PET-PAN-B is higher than the same counting for samples A and C, and inversely, the PAN fiber count for PET-PAN-B is lower than the same counting for samples A and C. Estimation of the pore volume of the PET-PAN composite mats shows that it is above 81 % for all samples (Table 3). The relatively large standard deviation of the pore volume measurements makes them statistically indistinguishable (Table 3). The tortuosity, which is a description of the winding nature of the pores within the materials, is comparable in all samples and indicates relatively direct pathways through the fibers.

We evaluated the filter efficiency of each PET-PAN mat by challenging them with an aerosol of DEHS, with the efficiency being defined as the percentage of particles that are retained by the filter medium (Eq. (2)). In aerosol filtration, besides efficiency, the dimensionless quantity α (alpha) is a critical parameter that quantifies the filter's ability to remove particles relative to the pressure it imposes on the air stream. It is calculated from the pressure loss before and after the filter membrane and the achieved efficiency (in this case, for a particle size of 0.3 µm and an air face velocity of 0.0533 m/s), according to the Eq. (4):

$$\alpha = 10.000 \times \left(\frac{-\log\left(1 - \frac{\mathrm{Eff}(\%)}{100}\right)}{d_p \times 9.98} \right) \tag{4}$$

where d_p (µm) is the DEHS particle diameter (0.3 µm), and 9.98 is a numerical constant that incorporates unit conversions and the factor $4/\pi$ from the ideal-fiber model [24]. In our experiments, we found that the lowest efficiency and alpha values were observed when the amount of PAN fibers is smaller, in the order: PET-PAN-A $<$ PET-PAN-B $<$ PET-PAN-C (Table 4). We estimated the permeability values from the experiments (k_{exp}) and it drops from 1.7 to 0.9 µm^2 across the series, consistent with the rising pressure drop.

We performed fluid flow simulations using the volumetric XRM data. To reduce computation time, we divided each dataset into three subvolumes (Figure 5A–C, i, ii and iii) and averaged the permeability results (Table 4, Figure S7). The simulated values (k_{sim}) were found to reproduce the same trend as the experimental values (k_{exp}) and stayed within the experimental uncertainty, with deviations of less than 35 % for PET-PAN-A and PET-PAN-C, and within the larger error bar of B. The streamlines (Figure 5D–F and Supplementary Videos) provide a clear illustration of the fluid flow paths within the simulated environment, and show slight differences among the samples, particularly where the fibers are more densely packed. PET-PAN-A (no DBCP) shows wide, nearly straight channels (Figure 5D iii) that bypass the fiber network, in agreement with low efficiency at the highest permeability (Table 4). PET-PAN-B (with DBCP) has PET bundles that produce very tortuous paths (Figure 5E iii), but also regions with more uniformly distributed streamlines with well-dispersed nanofibers that break up the large PET pores (Figure 5E i, ii), forcing air to sweep over more surface area. This lifts efficiency to 51 % while the pressure drop increases by only 4 Pa, giving the best gain in α, increasing from 7.9 in PET-PAN-A to 12.3 in PET-PAN-B. PET-PAN-C (double PAN with DBCP) shows PAN fibers better distributed, which further partition the flow. The result is the highest efficiency (72 %) but also the greatest pressure drop (44 Pa) and the lowest permeability (0.9 µm^2).

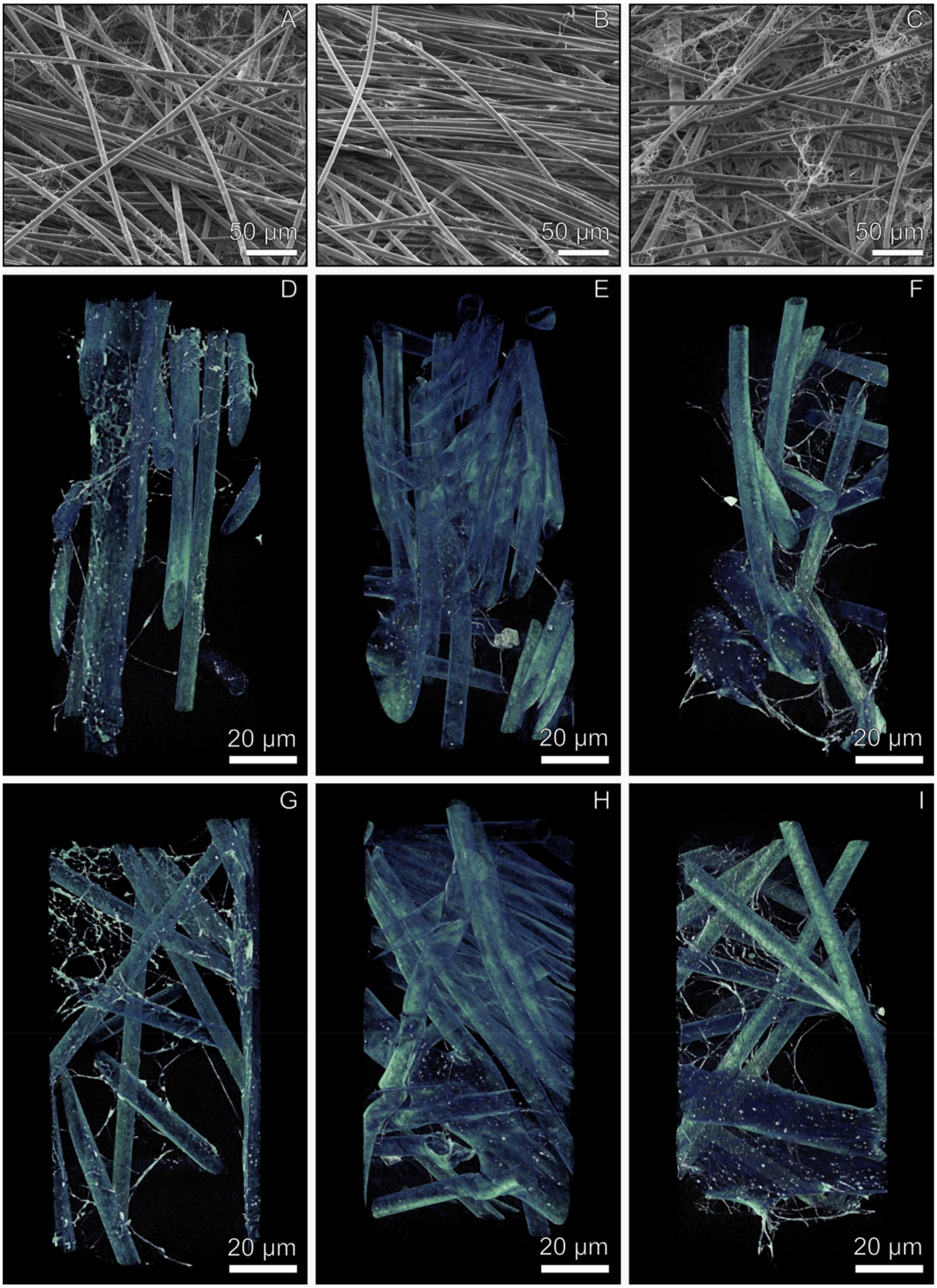

Figure 3: Electron and X-ray microscopy of the PET-PAN composite filter mats. SEM images of (A) PET-PAN-A, (B) PET-PAN-B and (C) PET-PAN-C. X-ray volumetric reconstruction of (D, G) PET-PAN-A, (E, H) PET-PAN-B and (F, I) PET-PAN-C with a side and top view, respectively.

Table 2: Structural features of PET–PAN filter mats that can be resolved by SEM versus XRM.

Filter sample	Fiber	SEM observations	XRM observations
PET-PAN-A	PET	Form a closed-mesh structure	Form an open-mesh structure with large pores
	PAN	Appear in localized regions, forming small agglomerates	Fibers predominantly attached to PET fiber surface, making smaller pores
PET-PAN-B	PET	Form a closed-mesh structure with high coverage	Form a closed-mesh structure with high coverage
	PAN	Form sparse agglomerates between PET fibers	Fibers sparsely visible across the volume
PET-PAN-C	PET	Form a closed-mesh structure	Form an open-mesh structure with large pores
	PAN	Extensively distributed; form a few agglomerates covering and in between the PET fibers	Fibers covering and in between the PET fibers, making smaller pores

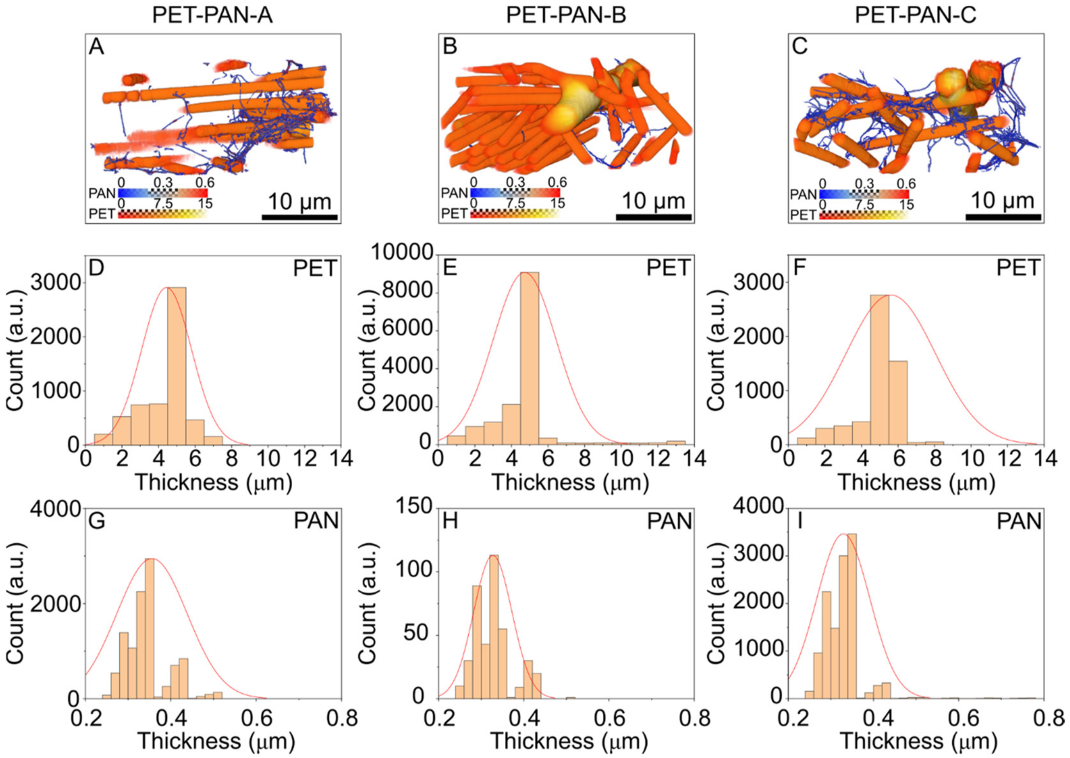

Figure 4: Fiber thickness distribution in PET-PAN composite filter mats. (A–C) Volumetric fiber thickness maps for samples PET-PAN-A, -B, and -C, respectively (color bars indicate fiber diameter in μm). (D–F) Histograms of the diameter of PET fibers for the same three samples. (G–I) Histograms of the PAN nanofibers for the same three samples.

4 Discussion

We fabricated composite mats comprising coarse PET fibers with electrospun PAN nanofibers in between, which divide the large pores created by the PET structure into finer channels. The PAN nanofibers substantially increase the specific surface area, thereby raising filtration efficiency without significantly increasing pressure drop. However, PAN nanofibers tend to agglomerate when processed in an aqueous medium. Therefore, we added an amphiphilic diblock copolymer (poly(AA_{94}-block-nBA_{58})). The hydrophobic n-butyl-acrylate (nBA) block tends to attach to the

Table 3: Morphological characteristics obtained with volumetric images of the PET-PAN mats.

Sample	PET thickness (μm)	PAN thickness (μm)	Pore volume (%)	Tortuosity
PET-PAN-A	5 ± 1	0.36 ± 0.08	89 ± 6	1.11 ± 0.08
PET-PAN-B	5 ± 2	0.33 ± 0.04	81 ± 11	1.15 ± 0.09
PET-PAN-C	6 ± 2	0.33 ± 0.06	86 ± 2	1.12 ± 0.06

surface of the predominantly hydrophobic PAN nanofibers due to the presence of nitrile groups [25], whereas the acrylic-acid (AA) block becomes negatively charged under mildly basic conditions. This introduces electrostatic repulsion that keeps the nanofibers dispersed. Thus, when present, the DBCP tailors the surface charge and surface energy of the hydrophobic electrospun PAN nanofibers. This ensures that electrostatic repulsion suppresses their aggregation. As a result, the PAN nanofibers are uniformly dispersed in the aqueous suspension during the wet-laid filter preparation (Figure 1). This homogeneous dispersion enables the short PAN fibers to separate the large pores created by the large PET fibers, yielding a hybrid fibrous network with narrower pores. During wet laying, the block copolymer adjusts the surface charge and surface energy of the hydrophobic electrospun short fibers, preventing them from clumping in the water-based fiber slurry.

We have used SEM and XRM to characterize the microstructure of the mats. These imaging techniques enabled detailed visualization of the morphology of the mats at microscopic scales, showing the PET fibers with PAN nanofibers unevenly distributed throughout the mats (Figures 3–5). SEM shows that sample PET-PAN-A, prepared without the diblock copolymer, possesses the most open structure, consistent with its highest measured porosity estimated by XRM. The number of counts used in the fiber thickness calculation differs between samples PET-PAN-A and -C and sample PET-PAN-B, which is likely due to sampling bias caused by the mats' high heterogeneity at the microscale combined with the XRM's small field of view. The volume of the PET-PAN-B sample analyzed happened to intersect a PET-rich, PAN-poor region of the inherently heterogeneous mat. Consequently, the PET-PAN-B sample, the PET counts are inflated while the PAN counts are suppressed (Figure 4E and H). The estimated thickness of the PAN fibers in the PET-PAN mats differs from that of the pure PAN nanofibers, which is probably due to the agglomeration of the nanofibers, making automated fiber recognition more difficult.

Single-pass DEHS tests confirm the structural trends. PET-PAN-A has the lowest pressure drop (24 Pa) and the poorest efficiency (29 %). Adding DBCP (PET-PAN-B) increases efficiency to 51 % while only raising Δp by 4 Pa. Raising the PAN loading to 2 wt% (PET-PAN-C) pushes efficiency up to 72 %, but also raises Δp to 44 Pa, reflecting the lower permeability of the sample. The corresponding efficiency factor α increases from 7.9 (PET-PAN-A) to 12.3 (PET-PAN-B) and 14.4 (PET-PAN-C), highlighting the advantages of DBCP-assisted PAN dispersion to promote more uniform fiber distribution via surface charge repulsion [26]. The single-pass filtration test was chosen as it allows for rapid assessment of sample performance and can be used to provide a clear direction for material optimization. Here, it particularly emphasizes the advantage of combining higher PAN content with diblock copolymer to lower pressure drop. Moreover, it allows assignment of the filter to international classes (ISO 16890, EN 1822) [27] and comparison across products.

To enable a comparison between experimental and fluid flow simulation performed in the 3D XRM data, we estimated the permeability, which is a physical property of the porous material and depends on the structure of the pores, their connectivity, and size, but it is independent of the type of fluid flowing through the material. Permeability derived from pressure-drop data (k_{exp}), as a measure of how easily air can pass through the porous matrix [28], decreases from 1.7 μm^2 (PET-PAN-A) to 0.9 μm^2 (PET-PAN-C). Simulated permeabilities (k_{sim}) obtained from the XRM volumes follow the same order and lie within experimental uncertainties (Figure S8), although the absolute values for PET-PAN-B scatter widely because the scanned volume happened to intersect a PET-rich, PAN-poor region. This sampling bias illustrates the trade-off between the high resolution of XRM and its limited field of view: the imaged sub-volume ($\approx 10^7$

Table 4: PET-PAN mats filtration tests and simulations.

Sample	Experiment				Simulation
	Δp (Pa)	Efficiency (%)	Alpha	k_{exp} (μm^2)	k_{sim} (μm^2)
PET-PAN-A	24 ± 5	29.2	7.9	1.7 ± 0.4	1.1 ± 0.2
PET-PAN-B	28 ± 1	50.6	12.3	1.5 ± 0.2	1.3 ± 1.0
PET-PAN-C	44 ± 0	71.6	14.4	0.9 ± 0.1	0.7 ± 0.1

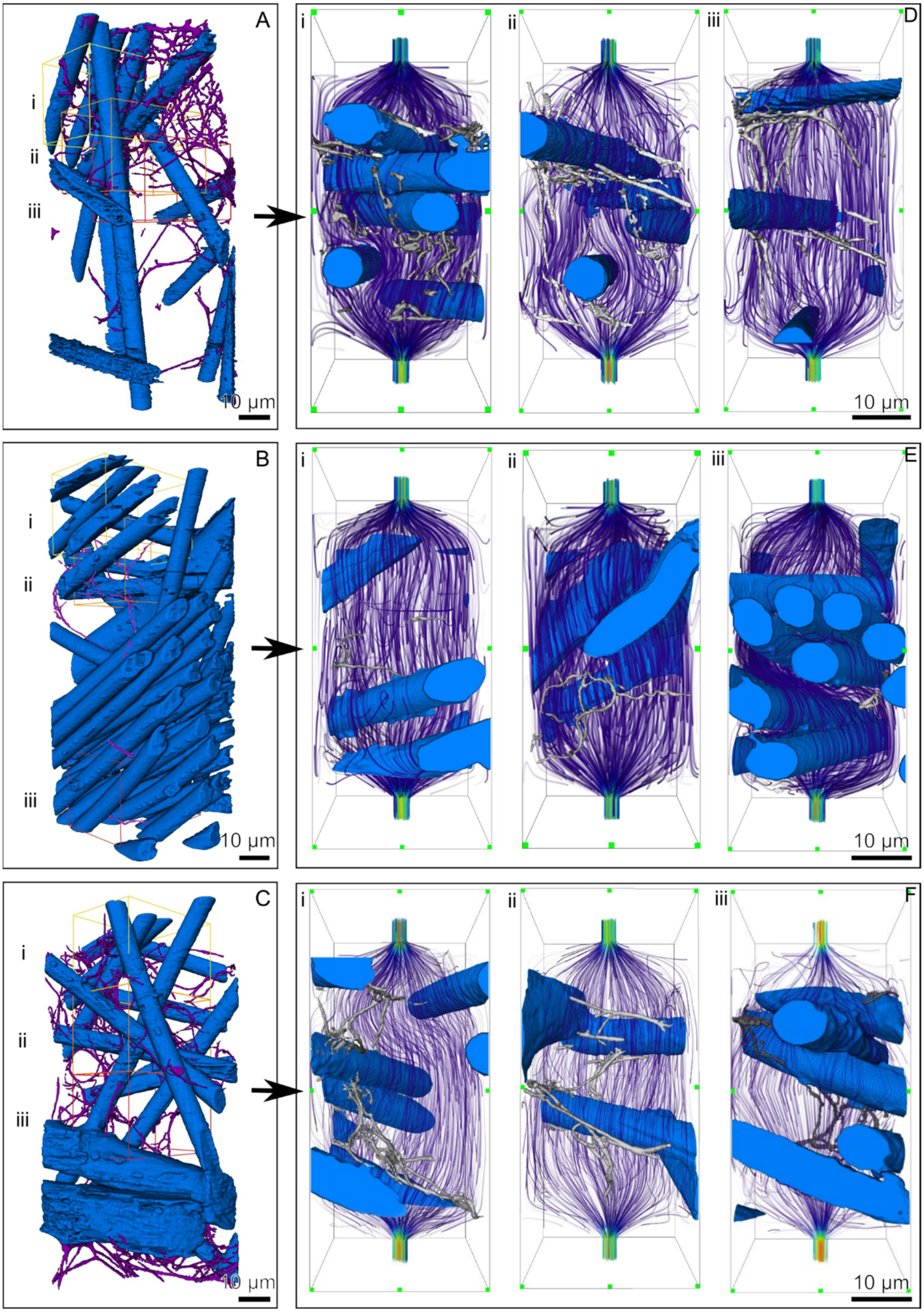

Figure 5: Volumetric reconstruction of PET-PAN mats, showing the small subvolumes (i, ii, and iii) used in the simulations of air flow: (A) PET-PAN-A, (B) PET-PAN-B and (C) PET-PAN-C. Corresponding representation of the flow streamlines through three representative subvolumes i, ii and iii, immediately on the right.

times smaller than the test sample) may not be fully representative of the bulk material that is heterogeneous at the microscale. This microscopic heterogeneity can result in localized variations in simulated permeability [15], [29], which may not adequately represent the experimental conditions as it may only capture a subset of these variations. The experimental setup, being larger, is more likely to capture a wider range of these heterogeneities, resulting in a more averaged permeability value. Also, smaller simulated volumes can create artificial boundaries that do not exist in larger experimental setups, affecting the results. Indeed, the size of the problem must be taken into consideration as it may limit the usability of the simulation method [30]. Enlarging the imaged volume by stitching together adjacent scans and repeating the flow simulation should provide a better representation of the experimental setup, but this can result in considerably higher data-handling and computational demands.

The discrepancy between the permeability simulated on a single high-resolution XRM sub-volume and the experimentally measured bulk value indicates that, for such heterogeneous mats, the scanned volume was smaller than the true representative volume element, so the local structure is not fully representative of the bulk. While this limits the method's ability to predict absolute Δp from a single scan, it simultaneously demonstrates quantitatively that microscale heterogeneity exerts a first-order control on macroscopic flow. The real strength of the simulation shown here, therefore, lies in its diagnostic power: by visualizing the flow fields in the 3D volume we can trace performance deviations back to concrete microstructural features such as fiber agglomeration or local porosity deficits. Recognizing microscale homogeneity as a central design lever provides a firm basis for developing next-generation filter media.

The XRM and simulation workflow presented here are fundamentally material-agnostic and can be readily adapted to other porous or fibrous systems, such as other polymer composites, ceramic fibers, or metallic foams, thus supporting and informing the design of efficient composite filtration mats. Future work should enlarge the sampled volume (stitching, multiple scan locations) or apply multi-scale modelling to convert these local insights into accurate bulk predictions.

5 Conclusions

We fabricated composite PET-PAN filter mats in which 5 μm PET fibers are overlaid with PAN nanofibers. Adding a small amount of nanofibers (1 wt%) alongside the DBCP increased the single-pass DEHS efficiency from 29 % (PET-PAN-A) to 51 % (PET-PAN-B), while only raising the pressure drop by 4 Pa. Increasing the PAN content to 2 wt% (PET-PAN-C) further improved the efficiency to 72 %, though this came at the price of a higher Δp of 44 Pa and a permeability reduction from around 1.5 μm^2 to 0.9 μm^2. SEM and XRM images agree with DBCP suppressing PAN agglomeration, producing a network that maximizes fiber surface area without severely narrowing the flow channels.

The XRM-based permeability simulation reproduced the experimental permeability trend and, more importantly, enabled the visualization of how local features such as agglomerates, porosity deficits and PET-rich domains influence the flow field. The discrepancy between the permeabilities obtained from high-resolution XRM volumes and those from bulk experimental tests shows that microscale heterogeneity dominates macroscopic resistance, and that larger volumes are needed for quantitative prediction. Nevertheless, the method's diagnostic capability already provides clear microstructure-to-performance links that can guide process adjustments.

These findings identify uniform nanofiber dispersion as the primary design lever for reaching a high ratio of efficiency to pressure-drop and show that XRM-based simulation is a versatile, material-agnostic tool for supporting the development of filter media. Future work should extend the imaged volumes and incorporate multi-scale modelling to translate the local insights obtained here into accurate bulk property predictions.

Acknowledgments: The authors thank Matthias Menzel at the Fraunhofer IMWS for the acquisition of SEM images. This work was partly carried out with the support of the Karlsruhe Nano Micro Facility (KNMF, www.knmf.kit.edu), a Helmholtz Research Infrastructure at Karlsruhe Institute of Technology (KIT, www.kit.edu). The Xradia 810 Ultra (nanoCT) core facility was supported (in part) by the 3DMM2O – Cluster of Excellence (EXC-2082/1390761711).

Research ethics: Not applicable.

Informed consent: Not applicable.

Author contributions: MIS: Validation, Formal analysis, Investigation, Writing – Original Draft, Visualization. JMSS: Conceptualization, Formal analysis, Writing – Original Draft, Visualization. DD: Investigation, Validation, Writing – Review & Editing. ML: Investigation, Validation, Writing – Review & Editing. RD: Investigation, Writing – Review & Editing. UH: Investigation, Formal analysis, Writing – Review & Editing. AG: Funding acquisition, Resources, Writing – Review & Editing. RBW: Funding acquisition, Resources, Writing – Review & Editing. All authors have accepted responsibility for the entire content of this manuscript and approved its submission.

Use of Large Language Models, AI and Machine Learning Tools: The language has been improved with ChatGPT 4.0.

Conflict of interest: The authors state no conflict of interest.

Research funding: The authors acknowledge the financial support of the German Ministry of Education and Research (BMBF) under the initiative "Biologisierung der Technik" via the project "PINGUIN" (grant number 13XP5180D). R.D. acknowledges the support by the Cluster of Excellence 3DMM2O (EXC-2082/1390761711) funded by the German Research Foundation (DFG).

Data availability: The data that support the findings of this study are available from the corresponding author, RBW, upon reasonable request.

References

[1] G. Liu *et al*., "A review of air filtration technologies for sustainable and healthy building ventilation," *Sustain. Cities Soc.*, vol. 32, pp. 375–96, 2017.

[2] S. Aziz *et al*., "A comprehensive review of membrane-based water filtration techniques," *Appl. Water Sci.*, vol. 14, no. 8, p. 169, 2024.

[3] L. M. Henning *et al*., "Review on Polymeric, Inorganic, and Composite Materials for Air Filters: From Processing to Properties," *Adv. Energy Sustain. Res.*, vol. 2, no. 5, p. 2100005, 2021.

[4] X. Zhang, J. Liu, X. Liu, C. Liu, and Q. Chen, "HEPA filters for airliner cabins: State of the art and future development," *Indoor Air*, vol. 32, no. 9, p. e13103, 2022.

[5] C. R. Gough *et al*., "Biopolymer-Based Filtration Materials," *ACS Omega*, vol. 6, no. 18, pp. 11804–12, 2021.

[6] S. Richter, J. Horstmann, K. Altmann, U. Braun, and C. Hagendorf, "A reference methodology for microplastic particle size distribution analysis: Sampling, filtration, and detection by optical microscopy and image processing," *Appl. Res.*, vol. 2, no. 4, p. e202200055, 2023.

[7] S. Alsoy Altinkaya, "A review on microfiltration membranes: fabrication, physical morphology, and fouling characterization techniques," *Front. Membr. Sci. Technol.*, vol. 3, 2024, https://doi.org/10.3389/frmst.2024.1426145.

[8] H. Roberge, P. Moreau, E. Couallier, and P. Abellan, "Determination of the key structural factors affecting permeability and selectivity of PAN and PES polymeric filtration membranes using 3D FIB/SEM," *J. Membr. Sci.*, vol. 653, p. 120530, 2022.

[9] Z. Pan *et al*., "High fidelity simulation of ultrafine PM filtration by multiscale fibrous media characterized by a combination of X-ray CT and FIB-SEM," *J. Membr. Sci.*, vol. 620, p. 118925, 2021.

[10] G. Rudolph-Schöpping *et al*., "Towards multiscale X-ray tomographic imaging in membrane science — A perspective," *J. Membr. Sci.*, vol. 690, p. 122245, 2024.

[11] S. C. Garcea, Y. Wang, and P. J. Withers, "X-ray computed tomography of polymer composites," *Compos. Sci. Technol.*, vol. 156, pp. 305–19, 2018.

[12] X. Liao *et al*., "High strength in combination with high toughness in robust and sustainable polymeric materials," *Science*, vol. 366, no. 6471, pp. 1376–9, 2019.

[13] C. Santos de Oliveira *et al*., "Direct three-dimensional imaging for morphological analysis of electrospun fibers with laboratory-based Zernike X-ray phase-contrast computed tomography," *Mater. Sci. Eng. C*, vol. 115, p. 111045, 2020.

[14] I. M. Griffiths, I. Mitevski, I. Vujkovac, M. R. Illingworth, and P. S. Stewart, "The role of tortuosity in filtration efficiency: A general network model for filtration," *J. Membr. Sci.*, vol. 598, p. 117664, 2020.

[15] L. Zhang *et al*., "The Investigation of Permeability Calculation Using Digital Core Simulation Technology," *Energies*, vol. 12, no. 17, p. 3273, 2019.

[16] T. Yasuda, S. Ookawara, S. Yoshikawa, and H. Matsumoto, "Materials processing model-driven discovery framework for porous materials using machine learning and genetic algorithm: A focus on optimization of permeability and filtration efficiency," *Chem. Eng. J.*, vol. 453, p. 139540, 2023.

[17] J. Bae *et al*., "Advancing Breathability of Respiratory Nanofilter by Optimizing Pore Structure and Alignment in Nanofiber Networks," *ACS Nano*, vol. 18, no. 2, pp. 1371–80, 2024.

[18] C. A. Schneider, W. S. Rasband, and K. W. Eliceiri, "NIH Image to ImageJ: 25 years of image analysis," *Nat. Methods*, vol. 9, no. 7, pp. 671–5, 2012.

[19] D. Paganin, S. C. Mayo, T. E. Gureyev, P. R. Miller, and S. W. Wilkins, "Simultaneous phase and amplitude extraction from a single defocused image of a homogeneous object," *J. Microsc.*, vol. 206, no. 1, pp. 33–40, 2002.

[20] T. Weitkamp, D. Haas, D. Wegrzynek, and A. Rack, "ANKAphase: software for single-distance phase retrieval from inline X-ray phase-contrast radiographs," *J. Synchrotron Radiat.*, vol. 18, no. 4, pp. 617–29, 2011.

[21] Thermo Scientific, *Avizo Software 2019 – User's Guide*, Germany, Konrad-Zuse-Zentrum für Informationstechnik Berlin (ZIB), 2019, pp. 705–709.

[22] J. L. Woodward, "Source Modeling – Discharge Rates," in *Reference Module in Chemistry, Molecular Sciences and Chemical Engineering*, Amsterdam, Elsevier, 2014.

[23] O. Colombani, M. Ruppel, F. Schubert, H. Zettl, D. V. Pergushov, and A. H. E. Müller, "Synthesis of Poly(n-butyl acrylate)-block-poly(acrylic acid) Diblock Copolymers by ATRP and Their Micellization in Water," *Macromolecules*, vol. 40, no. 12, pp. 4338–50, 2007.

[24] S. Chattopadhyay, T. A. Hatton, and G. C. Rutledge, "Aerosol filtration using electrospun cellulose acetate fibers," *J. Mater. Sci.*, vol. 51, no. 1, pp. 204–17, 2016.

[25] H. Liu and Y.-L. Hsieh, "Preparation of Water-Absorbing Polyacrylonitrile Nanofibrous Membrane," *Macromol. Rapid Commun.*, vol. 27, no. 2, pp. 142–5, 2006.

[26] O. Colombani *et al*., "Structure of Micelles of Poly(n-butyl acrylate)-block-poly(acrylic acid) Diblock Copolymers in Aqueous Solution," *Macromolecules*, vol. 40, no. 12, pp. 4351–62, 2007.

[27] International Organization for Standardization. "Hydraulic fluid power - Filters - Multi-pass method for evaluating filtration performance of a filter element," (ISO Standard No. 16889:2022), 2022.

[28] B. Callow, I. Falcon-Suarez, H. Marin-Moreno, J. M. Bull, and S. Ahmed, "Optimal X-ray micro-CT image based methods for

porosity and permeability quantification in heterogeneous sandstones," *Geophys. J. Int.*, vol. 223, no. 2, pp. 1210–29, 2020.

[29] Y. Lu, Y. Lu, T. Lu, B. Wang, G. Zeng, and X. Zhang, "Computing of Permeability Tensor and Seepage Flow Model of Intact Malan Loess by X-ray Computed Tomography," *Water*, vol. 15, no. 15, p. 2851, 2023.

[30] D. Krach and H. Steeb, "Comparing methods for permeability computation of porous materials and their limitations," *Proc. Appl. Math. Mech.*, vol. 23, no. 1, p. e202200225, 2023.

Supplementary Material: This article contains supplementary material (https://doi.org/10.1515/mim-2025-0005).